scientific reports

Check for updates

OPEN

Precision control of microstructure variation and tensile properties in dissimilar friction stir lap welding joints using an adjustable tool

Amlan Kar[1,2], Yoshiaki Morisada[2], Abhishek Sharma[2]✉ & Hidetoshi Fujii[2]✉

Friction-assisted plastic deformation at the joint interface is essential for achieving the desired joint properties in dissimilar friction stir lap welding (FSLW) of aluminum alloy (Al) with steel (Fe). This plastic deformation can be precisely controlled by using an adjustable tool, where shoulder and probe rotation speeds are independently controlled. This study explores the effect of microstructure evolution and probe rotation speed on the weld's interface morphology and tensile properties of FSLW joints between an aluminum alloy and steel using an adjustable tool. Microstructure evolution is influenced by inherent material properties and process-induced stress inhomogeneity. Grain refinement in Fe is more gradual compared to Al, which exhibits a homogenous microstructure. Lower probe rotation speeds lead to more significant grain refinement in Al, while increasing probe rotation speeds promote the formation of intermetallic compounds. An intercalated structure with varying fractions and morphology is observed across the joint interface in all welds. The controlled evolution of microstructure and the differences in intercalated structure formation at the weld interface are attributed to variations in shear strength. This study demonstrates the ability of an adjustable tool to tailor the microstructure and tensile properties of FSLW joints, providing a promising approach for enhancing joint performance in dissimilar metal joining applications.

Keywords Dissimilar friction stir lap welding, Adjustable too, Probe rotation speed, Microstructure evolution, Weld interface morphology, Shear strength, Intercalated structure

The friction stir welding (FSW) of dissimilar materials is very important in hybrid manufacturing, which is used in different aerospace and automobile industries. In hybrid manufacturing, the advantages of both materials are taken into consideration for a specific industrial application. The aluminum–steel lap members benefit from the individual properties of their constituent dissimilar materials: the high strength of steel and high specific strength of aluminum. However, the welding of such dissimilar materials as Al and Fe is very difficult due to the large difference in their melting points and the formation of brittle intermetallic compounds (IMC) at the interface. Conventional fusion welding, non-fusion welding and mechanical connection have been extensively used for fabrication. However, the resulting weld suffers from welding defects such as porosity, cracks and droplet spatter due to the enormous difference in the properties of aluminum and steel. These problems can be overcome by using a solid-state welding method and the joining of Al and Fe using ultrasonic welding[1], explosive bonding[2], and linear friction welding[3,4] has been extensively investigated.

In the recent past, friction stir welding (FSW) has been widely used for the dissimilar welding of Al to Fe because of its low energy input, short welding time, low distortion and relatively low welding temperatures[5,6]. Several studies demonstrate its ability to tailor interface morphology[7], microstructure evolution[8,9], and mechanical performance[7,10]. When sufficient heat exists, an atomic bonding happens between the aluminum and steel atoms. During the FSW process, the stirring induced by the tool and applied pressure break the oxide layers and IMC compounds (if formed) of the aluminium and steel surfaces. This leads to grain refinement[11], which is beneficial in enhancing mechanical properties due to the Hall–Petch strengthening effect. However, with the decrease in grain size, there is a substantial increase in the grain boundary area per unit volume[12]. Thus, the stored energy of the material increases during FSW/friction stir processing (FSP) and makes the microstructure unstable. Under the welding temperatures, the FSW/FSP-processed materials undergo recrystallization and

[1]Arbegast Materials Processing and Joining Laboratory (AMP), South Dakota School of Mines & Technology, Rapid, SD 57701, USA. [2]Joining & Welding Research Institute, The University of Osaka, Osaka 567-0047, Japan. ✉email: sharma.abhishek.jwri@osaka-u.ac.jp; fujii.hidetoshi.jwri@osaka-u.ac.jp

grain growth, which decides the final microstructure across the dissimilar weld. The variation in microstructure evolution across the weld influences and the relative strain inhomogeneity during tensile testing lead to a variation in the tensile properties, consequently[13].

In lap welding, the interaction of the tool probe with the steel plate plays an important role in the formation of the interface structure, intercalated interface, mechanically mixed zone (MMZ) and intermetallic compounds[12]. The welding parameters that affect interface formation are the plunge depth and probe rotation speed. The substantial deformation of the Fe plate during its friction stir lap welding (FSLW) to Al was studied by Wang et al.[14] using the friction stir scribe technology. The authors reported that the fracture mode and joint strength were greatly influenced by the interface structure and process parameters. In FSLW, the tool rotational speed and welding speed simultaneously affect the interface structure, IMC layer thickness, microstructure, tensile properties and fracture location of the welded joints. Kar et al.[15] showed that the interface structure influenced the formation of IMC layers during dissimilar welding. At the same welding speed, the IMC thickness decreased with an decrease in the rotating speed of the tool, resulting in an increase in the tensile fracture load. Therefore, the deformation of the Fe interface and corresponding microstructure evolution decide the final mechanical properties of the weld[16].

In the present investigation, friction stir lap welding of aluminum 6061-T6 with mild steel was carried out under varying probe rotation speeds while the shoulder rotation speed was held constant using an adjustable tool. This tool allowed the shoulder and the probe to operate independently. The friction at the shoulder-workpiece interface was found to be the predominant heat source, with minimal heat coming from the probe-workpiece contact. Notably, deformation at the interface, which is affected by the probe, was more significant due to the occurrence of deformation at lower temperatures. Enhancements in material flow around the Fe/Al interface were made possible by the increased probe rotation speeds using the adjustable tool, without markedly increasing the total heat due to the constant shoulder rotation speed. The application of shoulder rotation contributed to a reduction in tool wear and the adhesion of materials at the gap between the probe and shoulder, an advantage over the fixed shoulder approach. The employment of shoulder rotation mitigated tool wear and the sticking of materials at the gap between the probe and shoulder, which is an improvement over the fixed shoulder method. The study included a comprehensive analysis of the microstructural changes and mechanical properties of the welds to uncover the formation processes of different interface structures influenced by various probe rotation speeds at constant heat-input condition as shoulder adds no additional heat to the weld surface. The mechanical properties of the joints were examined. The results of this study elucidate the mechanism of formation of different interface structures at different probe rotation speeds and establish a correlation between the microstructures and properties of the welds. The findings provide insights into how to optimize the FSLW process for improved tensile properties of the welds.

Experimental procedure

Two millimetres thick aluminium alloy (AA 6061) and 2.0 mm thick mild steel (Fe; SPCC grade) sheets were selected as the base materials for dissimilar FSLW. The dissimilar FSLW of Al to Fe was performed using a adjustable FSW tool under the position control mode. The experimental configuration of FSW using the adjustable tool is displayed in Fig. 1(a), in which the Al 6061 alloy sheet was above the SPCC steel sheet. The diameter of the probe is 12 mm and the convex surface has a radius of 7 mm. Actual image of the adjustable tool is shown in Fig. 1(b) illustrating the assembly of tool shoulder and probe. The adjustable FSW tool was fabricated from H13 tool steel, heat-treated to approximately 52 HRC, which is having sufficient thermal stability and wear resistance for interaction with steel during dissimilar lap welding. Different components of the adjustable tool are illustrated in Fig. 1(c-d). It comprises a shoulder (Fig. 1(c)) and a probe (Fig. 1(d)). The shoulder is the portion of the tool that contacts the workpiece's top surface, playing a crucial role in generating heat. The probe is the component of the tool that penetrates the workpiece, causing deformation and generating the heat required for FSW. The complete assembly of the shoulder and probe in the adjustable tool is depicted in Fig. 1(e)). The probe diameter of 6 mm and probe length of 2 mm was used for the experiment. A tilt angle of the tool was 3° and a fixed plunge depth of 2.2 mm were adopted. The shoulder and the probe have the same rotation direction (clockwise rotation) with a welding speed of 100 mm/min. In order to investigate the influence of the adjustable tool on the mechanical properties of the welding joints, different rotation speeds of the shoulder and the probe were selected. In all experiments, the shoulder rotated at a constant 300 rpm while the probe rotation speed was varied (300, 1000, 1700 rpm). The independently driven rotation allowed decoupling the relative effect of heat input from deformation at the interface. The shoulder has a concave surface, and the probe has a convex profile with a single-start square thread (pitch: 0.3 mm, thread depth: 0.5 mm, and thread length: 2 mm). The threaded probe design was expected to facilitate effective mechanical interlocking and material flow, particularly at the Al/Fe interface. Since shoulder rotation is the primary source of heat-input to the weld, it was kept constant. To find the effect of probe driven deformation, probe rotation was varied during the experiment. This adopted methodology is expected to improve the deformation at the welding interface and leading to mechanical mixing and better joining of dissimilar materials. The selected plunge depth (2.2 mm) was more than the thickness of the top Al plate and hence, the tool probe interacted with the bottom Fe plate by 0.2 mm. Therefore, a weld interface developed along with severe deformation of Al and Fe across the weld.

After welding, the weld plate was sectioned using electro-discharge machining (EDM) and the metallographic specimen and shear tensile test specimen were obtained (width of 20 mm). The weld samples were polished by the standard metallographic method and subsequently etched by Keller's reagent for aluminum after final polish with 1 μm Al_2O_3 suspensions. The polished and etched samples were examined by optical microscopy and scanning electron microscope (SEM). For selected samples, for example, in Fig. 2, a light etching of the steel side was performed using 2% Nital solution for a few seconds, in addition to Keller's reagent for Al. This selective preferential etching approach was adopted to visualize the variation in microstructure evolution and

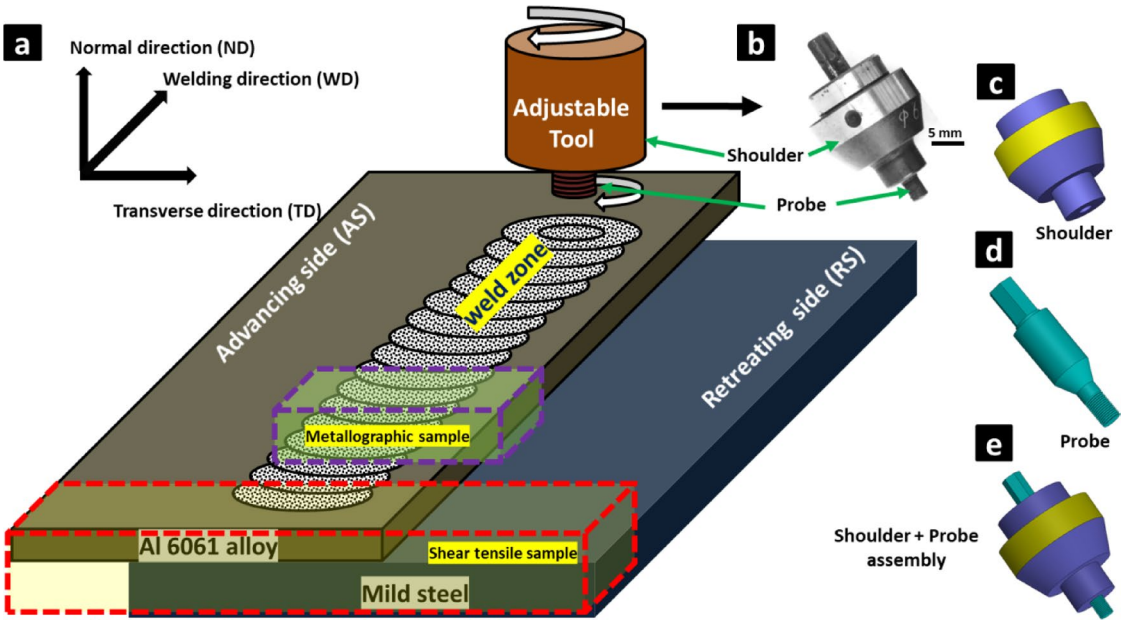

Fig. 1. **a)** Schematic illustration of experimental arrangement showing adjustable FSW tool with independently rotating shoulder and probe; and **b**) image of adjustable tool showing assembly of tool shoulder and probe. Schematic representation of different parts of the adjustable tool showing **c**) shoulder, **d**) probe and **e**) assembly of tool. The schematic illustrates an independently rotating tool shoulder and probe. The shoulder serves as the primary heat source (300 rpm), while probe speeds were adjusted to control interfacial deformation.

deformation at the Al/Fe interface. However, for other figures, etching was done only with Keller's reagent, targeting the Al side. As a result, steel grains are not visible in those micrographs.

The electron backscatter diffraction (EBSD)-based investigations were carried out using the TSL (Tex Sem Lab) data acquisition system fitted with a tungsten gun scanning electron microscope (GSEM). The instrument used was the ESEM quanta-200 model from FEI. The data analyses were carried out using the EDAX Tex-SEM TSL-OIM (version 7.1) data analysis software. The EBSD data were represented in the form of inverse pole figure (IPF) maps that show the position of a sample direction relative to the crystal reference frame. In addition, phase maps were generated wherever required. The commonly used grain-based parameter is the grain orientation spread (GOS). In GOS, the deviation of the average orientation of a grain from the orientation of each individual measurement point within the grain is calculated. It is a measure of the strain gradient within the grain[17]. The GOS of a recrystallized grain is usually less than 2° and that of a deformed grain is above 4–5°. The local variation in misorientation is commonly used as a measure of the strain in deformed microstructures. The kernel-based and grain-based approaches are the two major types to represent intra-granular misorientations. The commonly used kernel-based parameter is the kernel average misorientation (KAM), which represents the average misorientation between a point (which depends on the step size of the EBSD scan) in the scan at the center of the kernel and all points in its perimeter (its neighboring points). The average misorientation value is assigned as the KAM of the center point. For grain-based approaches, A grain average misorientation (GAM) map has been generated. GAM is a type of orientation map use to visualize the misorientation distribution within individual grains in a polycrystalline material. GAM maps are typically generated by calculating the average misorientation between all neighboring points within a grain and assigning a color to each pixel based on the calculated misorientation angle.

To study the phases present in the weld, x-ray diffraction (XRD) measurements were performed with the 2θ angle between 25° and 90° with CuK_{α} radiation (1.541 Å). A manual program was used to perform the scan at the center of the weld with a spot size of 1 mm in diameter. The x-ray analyses were conducted for all the samples presented in this study. The data obtained from XRD measurements were analyzed by the X'Pert Highscore PANalytical software. Some shear tensile tests were carried out in order to evaluate the mechanical properties of the joint. Location of the weld from where shear tensile specimens were sectioned is schematically shown in Fig. 1. The length and width of shear tensile sample were 175 mm (consider sheet overlap of 25 mm) and 20 mm, respectively. These tests were performed at room temperature at a strain rate of 1 mm/min using an Instron-based testing machine with a crosshead speed of 1 mm/min. For each welding condition, five shear tensile samples were tested. The fracture surface of the tensile samples was analyzed using a SEM.

Results and discussion

Variation in microstructure evolution

Low-magnification optical microscopy was used to visualize the entire weld interface and deformation of the material at the advancing side (AS) and retreating side (RS) of the weld. In the following images, the left side

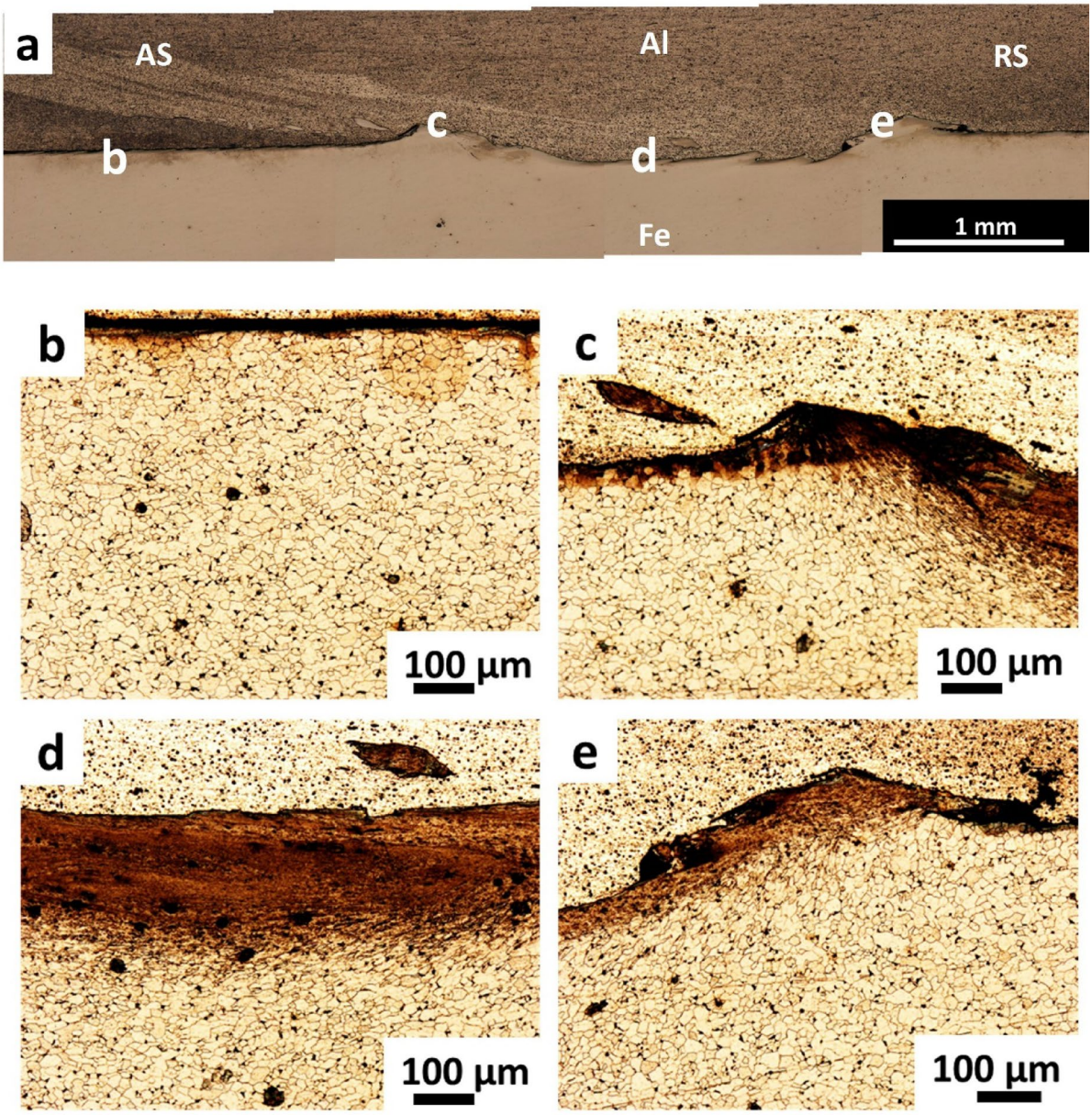

Fig. 2. Evolution of microstructure of the weld with probe rotation speed of 300 rpm exhibiting optical micrographs at different location of the welds.

shows the AS of the weld, and the right side shows the RS. Figure 2(a) shows the optical macrostructure of the weld with probe rotation speed of 300 rpm, with detailed characterization of the interface using an optical microscope at the locations indicated. The optical microstructure of the as-received Fe is shown in Fig. 2(b). This location is far from the interaction zone, and hence, no deformation is observed. Deformation at the interface of Fe due to the difference in chemical etching is noticed at the AS (Fig. 2(b)), middle (Fig. 2(c)), and RS (Fig. 2(d)) of the interaction zone. The middle of the Fe interaction zone is more severely deformed than the other two zones. Interestingly, no fracture or crack is identified in the Fe interface. In the AS of the weld, an additional zone with a number of Fe particles is noticed. Wang et al.[18] has shown that the deformation of the Fe interface is caused by the shear stresses generated by the rotating probe. The shear stresses are highest in the middle of the interaction zone, where the probe rotation speed is highest. This explains why the middle of the Fe interaction zone is more severely deformed than the other two zones.

With the increase in probe rotation speed from 300 rpm to 1000 rpm, a change in interface morphology is noticed, as shown in Fig. 3(a). Fragmentation of the Fe interface is also identified at different locations of the weld interface (Fig. 3(b-d)). The lines of fragmentation are oriented parallel to the interface, and this direction of orientation is considered the direction of shear deformation. In the AS of the weld interface, the size of the particles is bigger (Fig. 3(e)) when compared to that seen in Fig. 2. Kar et al.[19] suggests that the fragmentation of the Fe interface is caused by the combination of shear stresses and thermal stresses. The shear stresses break up

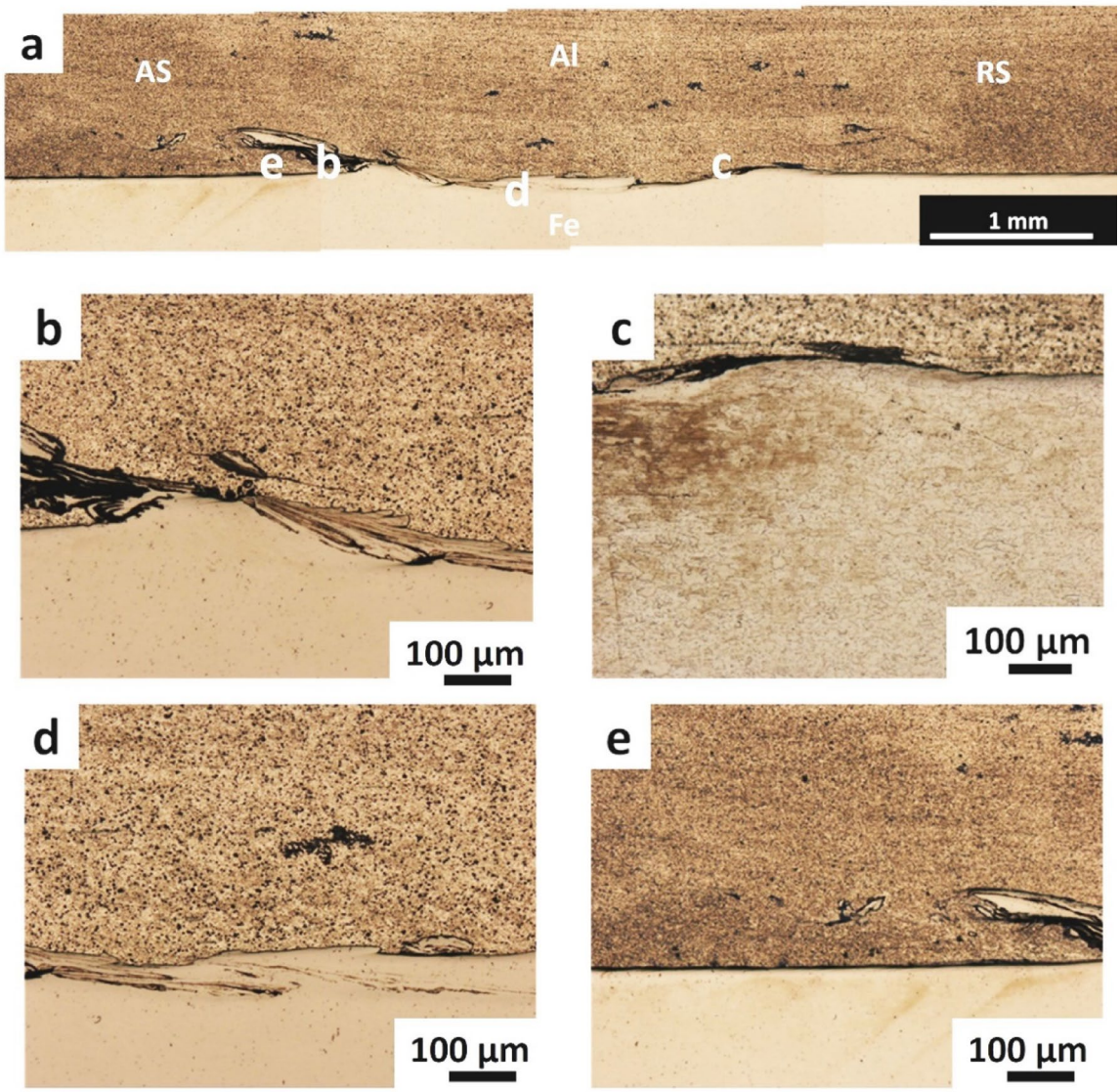

Fig. 3. Evolution of microstructure of the weld with probe rotation speed of 1000 rpm exhibiting optical micrographs at different location of the welds.

the Fe interface into smaller particles, while the thermal stresses cause these particles to coalesce. This explains why the size of the particles in the AS of the weld interface is bigger than in the middle of the interaction zone.

At a higher probe rotation of 1700 rpm, a wider interface is noticed, as seen in Fig. 4(a). A severe deformation and fragmentation zone is noticed across the Al/Fe interface, especially at the two edges and middle of the interface (Fig. 4(b-c)). The center (Fig. 4(d)) and two extreme edges (Fig. 4(e)) of the weld interface exhibit discrete black zones. These zones are predicted to be the zones of elemental mixing developed due to differential chemical etching within this zone. This kind of zone of elemental mixing is not observed in the weld with probe rotation speeds of 300 rpm (Fig. 2) and 1000 rpm (Fig. 3). Higher probe rotation speed and corresponding severe deformation are predicted to be the origin of such elemental mixing[12]. Kar et. al[19]. indicates that elemental mixing at the Al/Fe interface is caused by the diffusion of Al and Fe across the interface. The diffusion rate is increased by the high temperatures and shear stresses generated by the rotating probe. This explains why the zones of elemental mixing are only observed at the highest probe rotation speed.

Microstructure of weld interface

The microstructure of the welds with different probe rotation speeds was characterized in detail using SEM. The SEM micrographs of the welds corresponding to probe rotation speeds of 300 rpm (Fig. 5 (a)), 1000 rpm (Fig. 5 (b)) and 1700 rpm (Fig. 5 (c)) were characterized. At a lower probe rotation speed (300 rpm), the weld contained a large number of coarse Fe particles. A number of cracks were visible in the particles. In addition, extended cracks within particles and an onset of fracture were also noticed. These cracks could have developed during the formation of the particle from the Fe interface or during deformation after getting separated from the Fe faying interface. With an increase in the probe rotation speed, from 300 rpm to 1000 rpm, a severe deformation

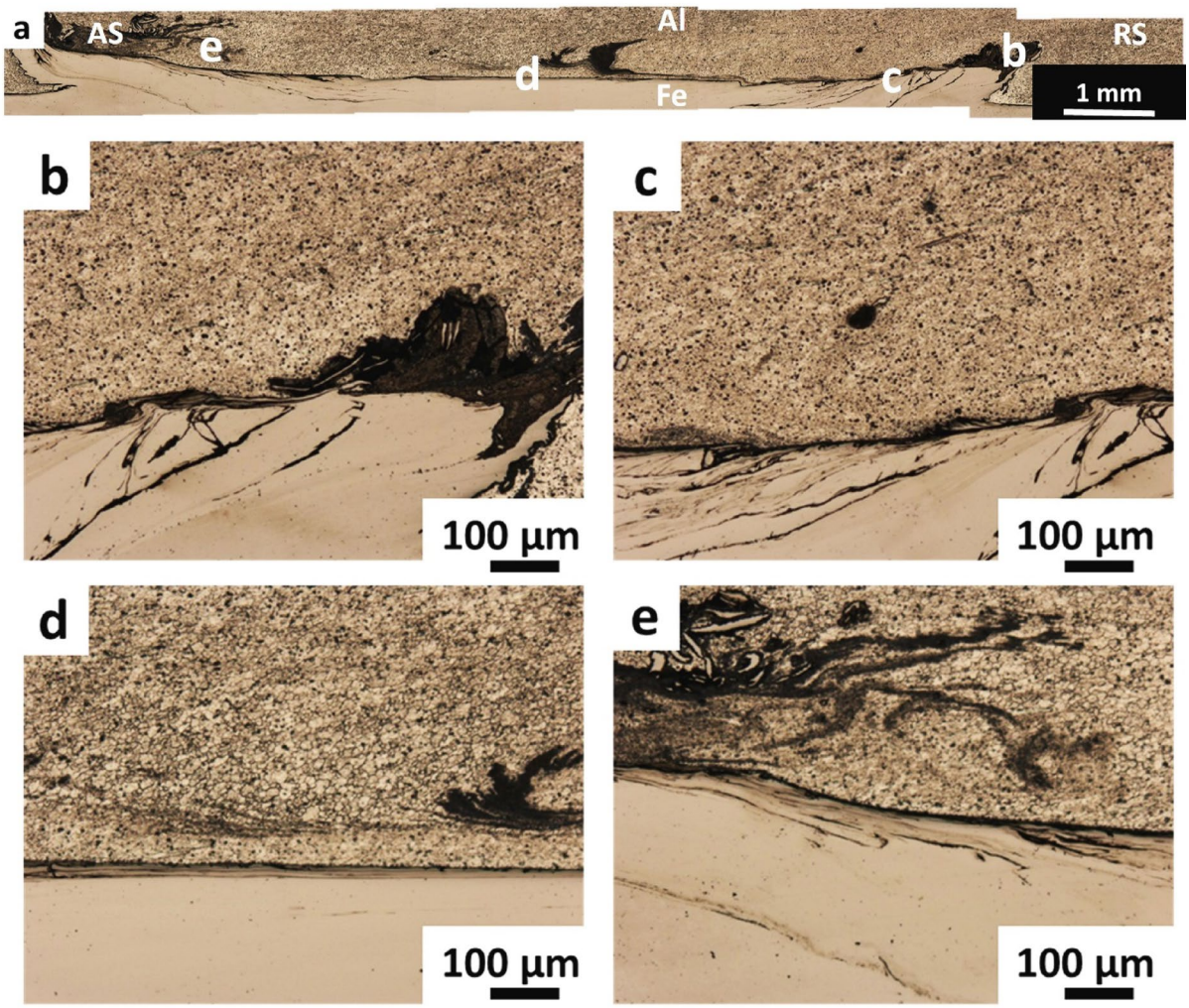

Fig. 4. Evolution of microstructure of the weld with probe rotation speed of 1700 rpm exhibiting optical micrographs at different location of the welds.

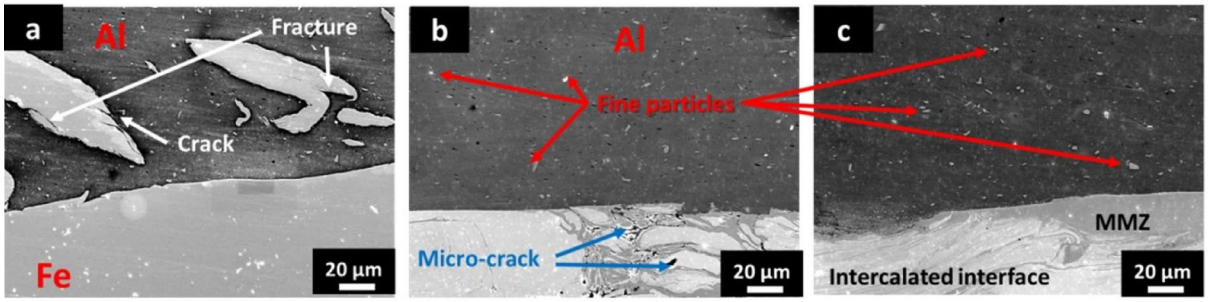

Fig. 5. **a)** SEM micrographs of the weld with probe rotation speed of 300 rpm, **b**) 1000 rpm, and **c**) 1700 rpm.

in Fe adjacent to the joint interface was noticed (as shown in Fig. 5 (b)). Such deformation in Fe leads to the development of micro-cracks and a possible reaction layer at the weld interface. In this deformation zone, both Al and Fe are interlocked with each other; this structure is termed as the intercalated structure in literature[20]. An identical intercalated structure was seen in the weld corresponding to a probe rotation speed of 1700 rpm. However, an additional mechanically mixed zone (MMZ) also developed adjacent to the intercalated zone (as shown in Fig. 5(c)). The MMZ in a friction stir weld is a region where the two parent materials are mixed together by the mechanical action of the rotating tool. It is formed by the generation of heat and friction at the weld interface, which plasticizes the parent materials[21]. The tool then stirs the plasticized materials together, creating

a vortex flow that breaks them up into small grains and mixes them together. The heat and pressure from the tool then solidify the mixed material into a solid weld. The width of the MMZ can vary depending on the welding parameters and the properties of the parent materials, but it is typically on the order of a few millimeters[22–24]. For instance, a higher tool rotation speed or a slower welding speed can lead to an expansion of the MMZ[18,19]. The mechanism of formation of different structures at different probe rotation speeds was attributed to the continuous fragmentation of Fe at the interface into comparatively finer particles and the formation of cracks that lead to a fracture in Fe.

To investigate the chemical composition and assess elemental mixing in the weld nugget, EDS mapping and line scan analyses were conducted for the weld interface at 1700 rpm, where extensive deformation occurs, leading to elemental variation and severe plastic strain. Figure 6 presents SE images and EDS dot maps for Fe, Al, and Mg across the weld interface at a probe rotation speed of 1700 rpm. The SE image (Fig. 6(a)) clearly distinguishes two distinct regions at the Al/Fe interface: a mechanically mixed zone (MMZ) and an intercalated zone. The MMZ was formed due to intense mechanical stirring and material mixing without the formation of intermetallic compounds, owing to insufficient temperature rise in Al and slow diffusion kinetics. The intercalated zone is characterized by a layered flow of Al and Fe phases resulting from severe plastic deformation and elemental diffusion caused by comparatively higher interface temperatures. These features confirm that high-strain localization occurred at the interface, facilitating intense deformation, mechanical mixing, localized diffusion, IMC formation, and fragmentation.

The corresponding elemental maps support these observations. The Al map (Fig. 6(b)) shows reduced intensity in the MMZ near the Al side of the weld. The uniform intensity in the MMZ indicates the absence of a chemical concentration gradient, suggesting that this zone was formed not only by diffusion but also by three-dimensional mixing due to probe rotation. Similarly, the Fe map (Fig. 6(c)) reveals the presence of Fe not only in the bottom region (steel) but also as embedded fragments within the MMZ, confirming Fe fragmentation and dispersion. It also shows that the particles distributed within the MMZ are Fe-based. The Mg distribution (Fig. 6(d)) follows a similar pattern to the Al map, consistent with its role as an alloying element. These elemental distributions corroborate the combined effects of mechanical stirring and thermal activation in determining the interface structure and composition. The variation in chemical composition and alloying across the Al/Fe interface suggests that both mechanical mixing and chemical diffusion are active mechanisms during high-

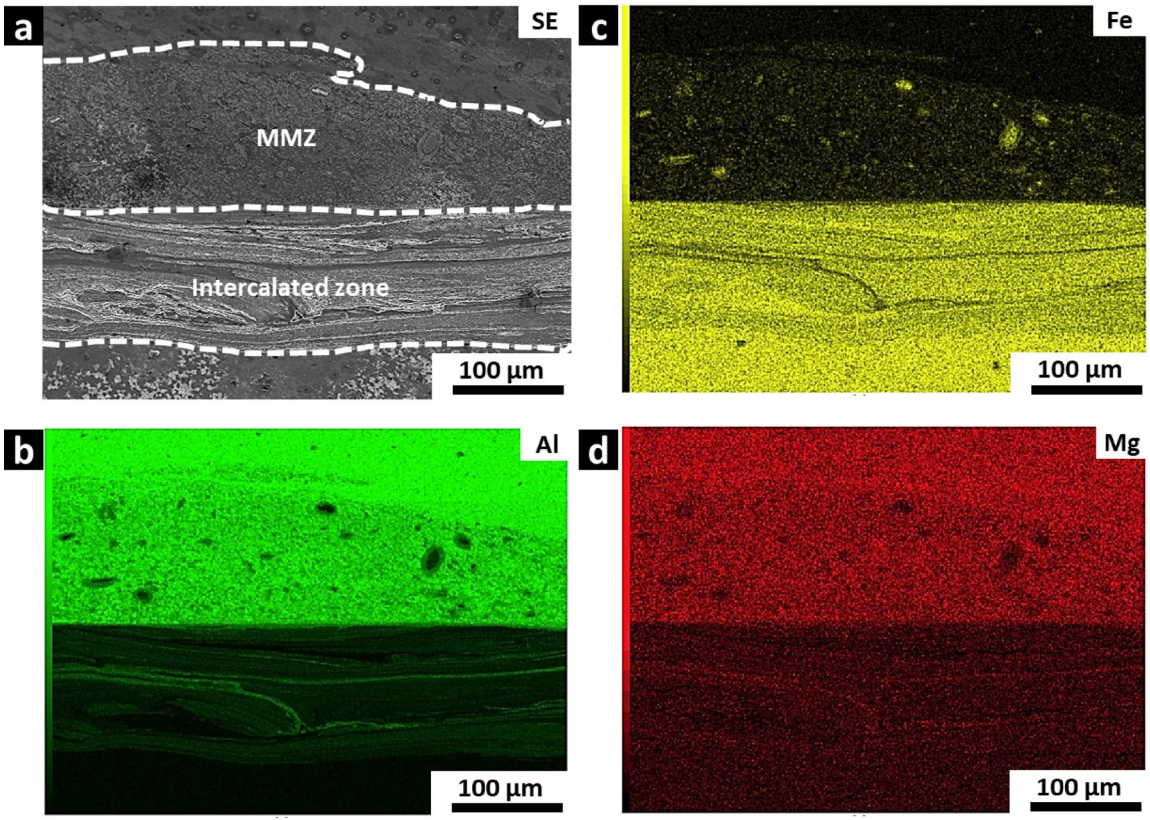

Fig. 6. (**a**) Secondary electron (SE) image of the weld interface corresponding to a probe rotation speed of 1700 rpm, showing the evolution of a well-defined intercalated zone and a mechanically mixed zone (MMZ) due to severe plastic deformation. EDS dot mapping illustrates the elemental distribution of (**b**) Al, (**c**) Fe, and (**d**) Mg across the interface. The maps reveal compositional variation across the interface and support the development of intercalated structures and an MMZ due to severe plastic deformation.

speed FSLW. Their relative activation contributes to the evolution of complex interfacial morphologies, which are expected to influence joint quality, IMC formation, and ultimately, joint performance.

To elucidate the chemical nature of the interface and the behavior of fragmented Fe particles, EDS line scan analysis was conducted on selected regions from the weld associated with a probe rotation speed of 1700 rpm, as shown in Fig. 7. Figure 7(a) shows a backscattered electron image of a fragmented Fe particle embedded in the Al matrix. The corresponding EDS line scan (Fig. 7(b)) indicates two transition regions at the Al/Fe interface of the particle. The central zone of the particle shows an Al-to-Fe atomic ratio consistent with the stoichiometry of $AlFe_3$. This clearly indicates that the fragmented particles were converted into intermetallic compounds (IMCs), which were eventually distributed within the mechanically mixed zone (MMZ) due to mechanical stirring caused by probe rotation.

Figure 7(c) shows the SEM image of the Al/Fe weld interface, with the red arrow indicating the line scan path across the reaction zone. The EDS profile in Fig. 7(d) reveals distinct elemental transitions from the Al-rich side into the Fe-rich domain across the weld interface. The region labeled "$AlFe_3$" represents a possible area in the intercalated zone where an IMC layer was formed. This region does not exhibit a steady concentration profile across the transitions, which extend over a spatial range of approximately 100 µm, suggesting that it consists of multiple layers. Some of these layers were converted into IMCs through diffusion followed by chemical reactions. The presence of $AlFe_3$ both in the interface zone and within the dispersed Fe particles implies that solid-state reactions and mechanical mixing under high strain and localized heating conditions generated by probe rotation were responsible for their formation.

Their coexistence is critical for the mechanical properties of the joint, as fragmented Fe and IMC particles embedded in the Al matrix could strengthen the weld through a dispersion hardening mechanism. However, the presence of continuous or thick intermetallic layers could also introduce brittleness, potentially leading to failure when the weld is subjected to shear tensile loading.

Microstructural evolution across interface

In addition to interface properties, a variation in the microstructure and residual stress across the interface play a significant role in the failure of welded structures[19]. Such variation is attributed to different crystal structures, physical and thermal properties of the materials to be welded. This variation leads to stress inhomogeneity across the interface during tensile testing and hence, there is a need to examine the possible location of the deformation that leads to fracture during tensile testing[25]. The position of the extended deformation decides the strength and

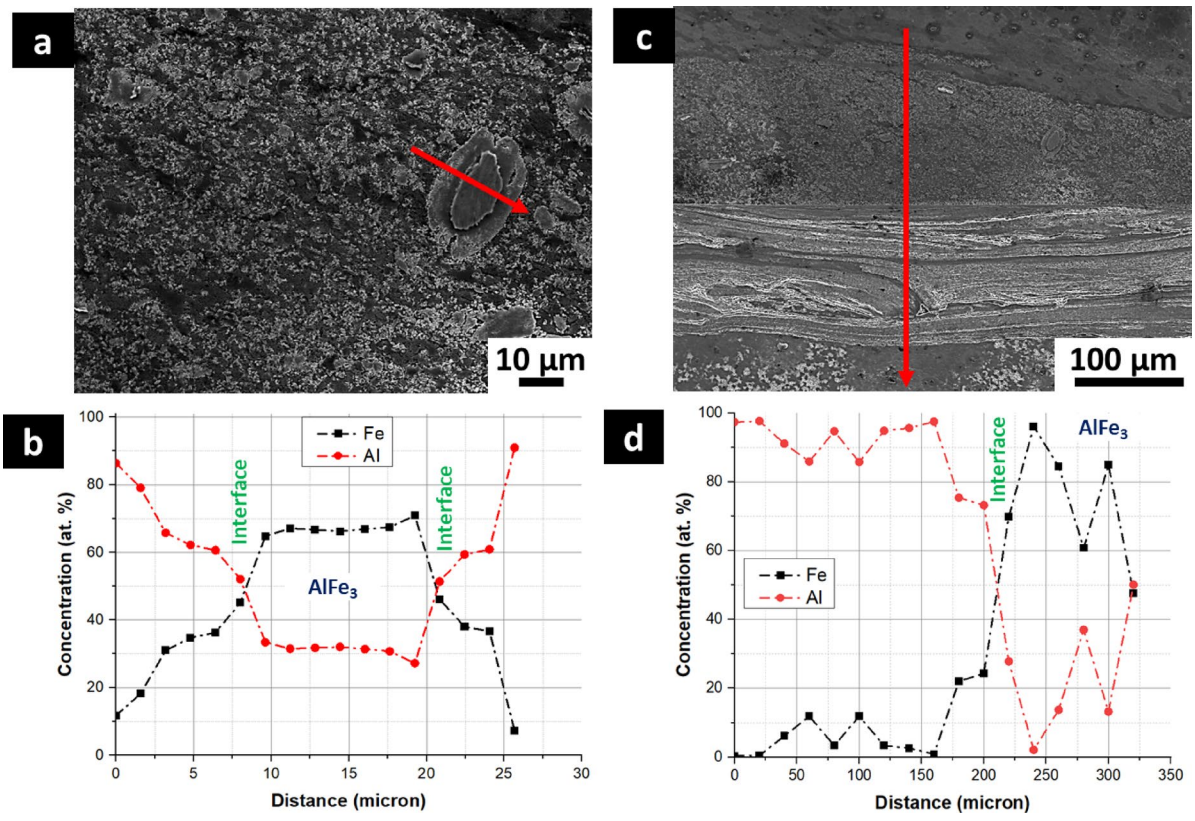

Fig. 7. EDS dot line scan analysis showing concentration profiles of Fe and Al across (**a**-**b**) fragmented particle embedded in the Al matrix and (**c**-**d**) weld interface associated with probe rotation speed of 1700 rpm resulting indication of possible formation of $AlFe_3$ IMC and development of MMZ in Al side of the weld adjacent to weld interface.

ductility of the weld if the interface of the weld is not the location of failure. Therefore, a detailed characterization of the variation in microstructure evolution across the interface is necessary.

Figure 8 shows the EBSD maps across the weld joint interface at extreme deformation condition i.e. at probe rotation of 1700 rpm. In the phase map in Fig. 8(a), three regions are demarcated: AA6061 (red colour), interlayer (in-between regions; black colour) and Fe (green colour). Figure 8(b) shows the IPF map of the same region. No preferential grain orientation was detected across the investigated region. The grains in AA6061 were coarser than that of Fe. Unlike Al, a gradient was seen in the microstructure on the Fe side of the interface. The Fe grain size increased with an increase in distance from the interface to the as-received Fe. Such a variation in grain size is due to the difference in thermo-mechanical deformation and microstructure evolution of Al and Fe on both sides of the interface, which induces a residual strain in the material[26]. To characterize the residual strain in the grains of both Al and Fe, a GOS map was generated. The Fig. 8(c) exhibits a low GOS value (blue region) in AA6061 as well as in Fe near the joint interface. These blue-coloured locations corresponding to a low GOS value can be considered as composed of recrystallized grains; this is because they indicate a low orientation deviation, which represents a low accumulation of dislocations. The results from the grain average misorientation (GAM) map, shown in Fig. 8(d), clearly indicated a higher value on the Fe side when compared to the AA6061 side from the weld interface. It illustrates that the dynamic recrystallization (CDRX) is the likely mechanism of microstructural evolution in Al whereas a gradual strain indued deformation influences microstructural evolution in Fe. The gradient in the strain beyond a critical level resulted in formation of adiabatic shear bands (ASBs) at higher strain rate and low temperature deformation during FSLW[27]. The presence of ASBs was inferred from high local misorientation (GOS > 4° and GAM > 2°) and directional fragmentation patterns in Fe (Fig. 8d). ASBs are deformation-localized zones formed at high strain rates and are commonly associated with micro-crack initiation[7,8].

The direction of ASBs was easy path for development of micro-cracks at the interfacial Fe and already made particles that were distributed in the weld nugget[22]. The development of these micro-cracks led to the

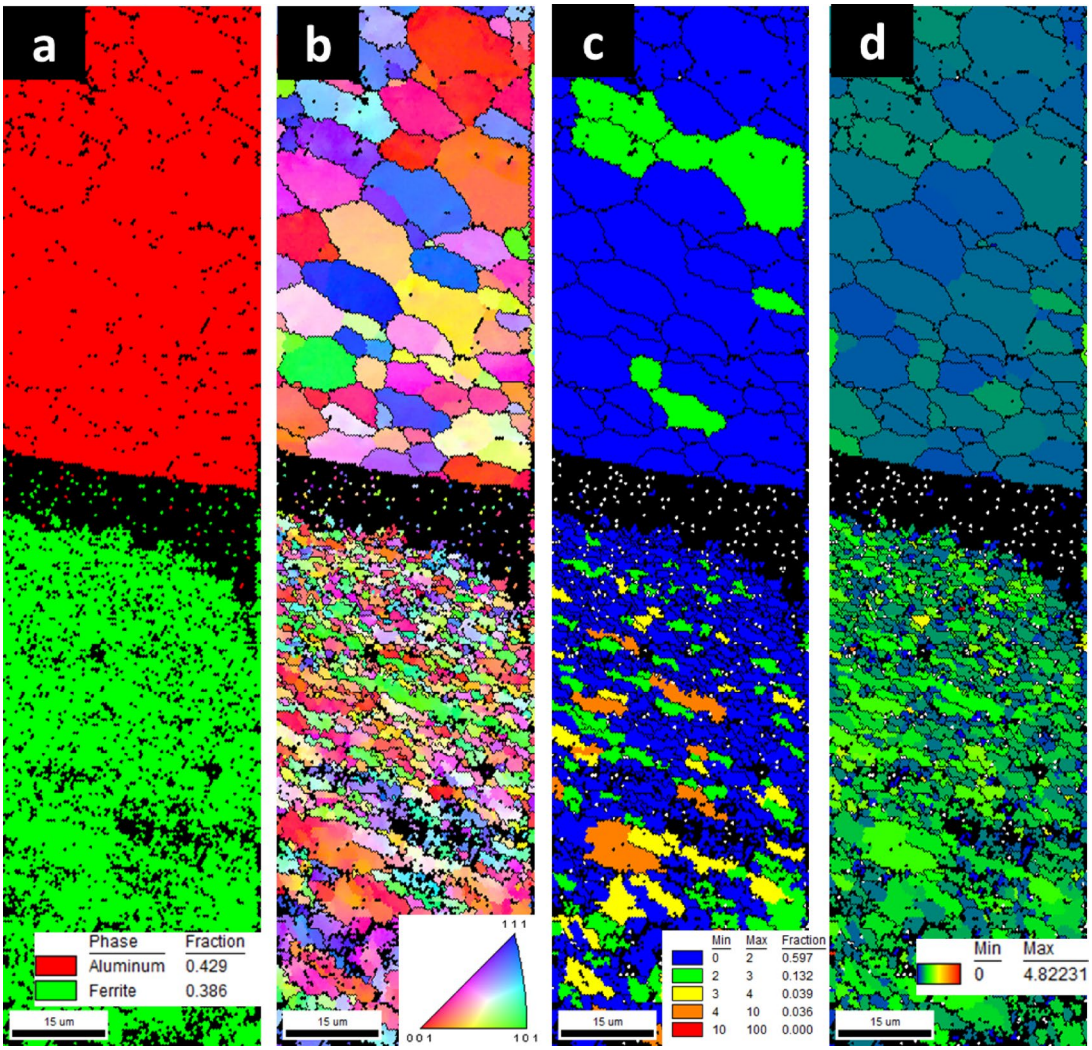

Fig. 8. EBSD-generated (**a**) phase map, (**b**) IPF map, (**c**) GOS map and (**d**) GAM map corresponding to probe rotation speed of 1700 rpm.

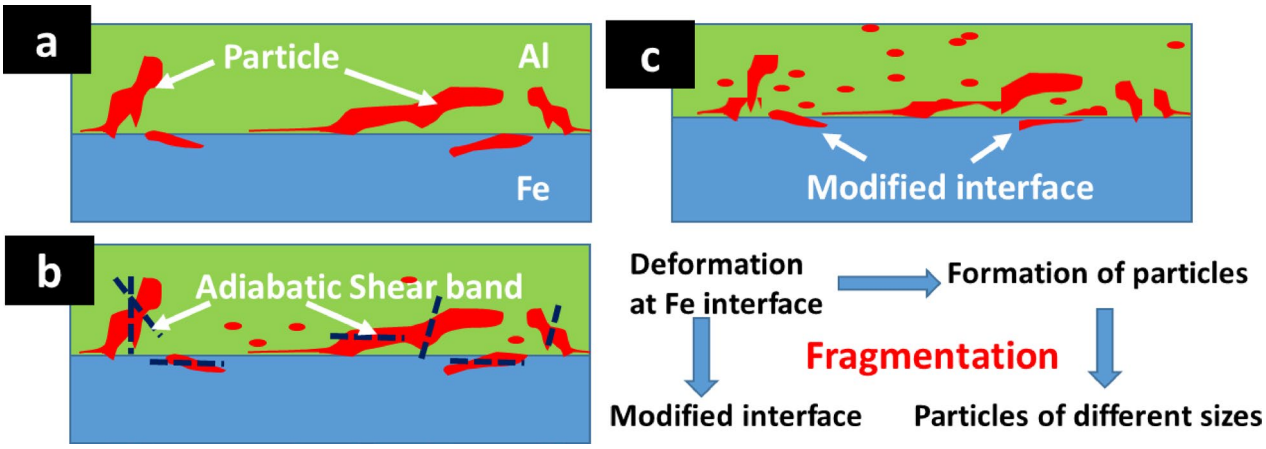

Fig. 9. Schematic representation of deformation and fragmentation of Fe during FSLW, (**a**) deformation of Fe interface and formation of particles, (**b**) development of adiabatic shear bands on interface and particle leading to continuous fragmentation and (**c**) weld morphology after the completion of the process.

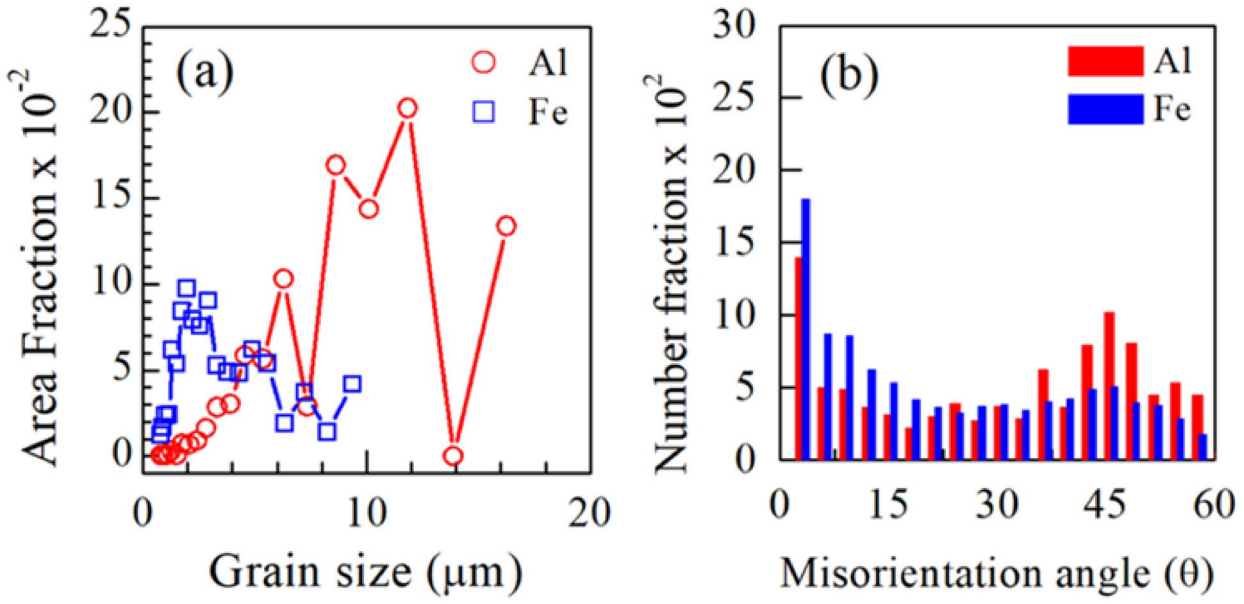

Fig. 10. EBSD-generated graphs across the weld showing (**a**) relative grain size distribution and (**b**) relative misorientation angle distribution of AA6061 (Al) and FE (Fe).

fragmentation. The fragmentation at the Fe interface resulted in formation of additional particles whereas particles of different sizes were developed due to fragmentation of already made particles[22]. The degree of deformation and continuous fragmentation generated different type of interface. The above-mentioned mechanism is schematically demonstrated in Fig. 9.

Figure 10(a) and Fig. 10(b) compare the grain size evolution and misorientation angle distribution respectively of AA6061 and Fe across the weld interface of the same scan; this weld corresponds to a probe rotation speed of 1700 rpm. It was found that the grain size of Fe (3 ± 1 μm) was substantially finer than that of Al (9 ± 3 μm). Furthermore, it is evident from Fig. 10(b) that the Fe microstructure contains a high fraction of low-angle grain boundaries (LAGBs) when compared to the weld interface adjacent to AA6061. The gradual decrease in the LAGB fraction with an increase in misorientation angle up to 15° (high-angle grain boundaries (HAGBs)) points to a mechanism of continuous substructure formation and its transformation to form recrystallized grains. A fraction of these substructures reduced with an increase in the misorientation angle. In addition, the evolution of a higher fraction of HAGBs in AA6061 compared to Fe illustrates the development of a higher fraction of recrystallized grains in AA6061. It also indicates a higher degree of thermo-mechanical deformation of Al, influencing the formation of final microstructure. Since AA6061 is a low-strength material when compared to Fe and it could lead to fracture during shear tensile testing, the microstructure of AA6061 could influence

the mechanical properties of the weld. Therefore, a detailed investigation on the microstructure of AA6061 is desired to predict the weld quality.

Further, the existence of the MMZ along the joint interface has been reported in literature[12,19]. An identical methodology was used by Kar et al.[12] to examine the mechanical mixing and material flow in dissimilar welds. The authors found that mechanical mixing at different length-scales influenced the interface properties and mechanical properties. A further detailed investigation of the SZ of AA6061 was carried out in order to understand the influence of microstructure on weld joint properties.

Microstructural evolution of al adjacent to interface

Across the interface, aluminum is subjected to severe thermo-mechanical deformation followed by microstructure evolution in comparison to steel; this is because the temperature of the weld is dictated by the lower melting point material, which is Al in the present couple. Further, Al is subjected to a higher degree of strain hardening than Fe due to its low tensile strength. Under severe deformation, Fe develops adiabatic shear bands (ASBs), which accommodate strain through local recrystallization and micro-crack formation. Therefore, it is essential to understand the difference in the microstructure under different processing conditions as it influences the final tensile properties of the dissimilar weld.

The microstructure of Al adjacent to the weld interface was studied with the help of EBSD. An IPF map and superimposed grain boundary map were generated for all the welds, as shown in Fig. 11. A substantial variation in grain orientation was observed with respect to the sample reference frame. From Fig. 11(a), it is seen that the grains corresponding to probe rotation speed of 300 rpm are oriented as <111> ‖ WD. An identical grain orientation was observed in the weld with rotation speed of 1000 rpm (Fig. 11(b)). However, an increase in the average grain size was also observed in the weld with rotation speed of 1000 rpm in comparison to that of 300 rpm. A mix of grain orientations such as <101> ‖ WD and <100> ‖ WD was noticed at the higher probe rotation speed of 1700 rpm (Fig. 11(c)). Such variation in microstructure evolution could influence the local shear deformation during shear tensile testing.

Figure 12(a) and Fig. 12(b) compare the grain evolution and misorientation angle distribution respectively of Al. The Fig. 12(a) shows the EBSD-generated grain size distribution of Al at the center of the Al sheet. The results indicated a substantial variation in the average grain size of Al at different probe rotation speeds. It was noticed that the grain size increases with an increase in the rotation speed. A substantial grain refinement (2 ± 0.8 µm) from the as-received grain size of Al (15 ± 5 µm) was identified at 300 rpm. The average grain size was substantial at the higher rotation speeds of 1000 and 1700 rpm. However, the variation in grain size was within the value of standard deviation. It was found that the grain size at all probe rotation speeds is much less than the as-received Al. This is due to the process-induced shear deformation of materials in the weld nugget. On the other hand, the Fig. 12(b) indicates a high fraction of LAGBs and HAGBs in the welds P1000 and P1700, respectively. It clearly exhibited a high fraction of substructure formation in P1000 compared to a high fraction of recrystallized grains with an accumulation of low number of dislocations in P1700.

Micro-texture evolution

Figure 13 shows the (111) pole figures representing the micro-textures measured from the surface of the weld at different probe rotation speeds of 300 rpm (Fig. 13(a)), 1000 rpm (Fig. 13(b)) and 1700 rpm (Fig. 13(c)). The pole figures were rotated about the axes in order to align the assumed shear plane normal (SPN)/welding direction (WD) vertical and shear direction (SD) horizontal. Since the deformation close to the probe is predominantly by simple shear, the shear texture components were detected from the pole figures. The grain orientations present were apparent $A/\bar{A}$ and B texture components for the weld corresponding to 300 rpm rotation speed (Fig. 13(a)) and B texture component for the welds corresponding to 1000 and 1700 rpm rotation speeds. In general, the shear deformation of face-centered cubic (FCC) metals occurs by gliding on the plane in the <110> direction. The first fiber, called **A** fiber, contains a {111} pole in the shear plane with the in-plane component randomly positioned; another fiber, called B fiber, is derived from the <110> shear direction where the shear plane

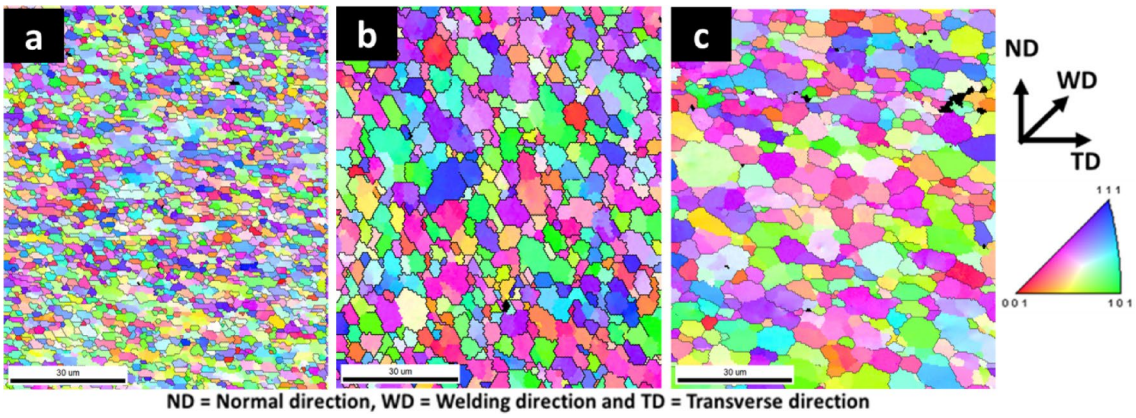

Fig. 11. EBSD-generated IPF map of Al adjacent to joint interface at probe rotation speed of (**a**) 300 rpm, (**b**) 1000 rpm and (**c**) 1700 rpm.

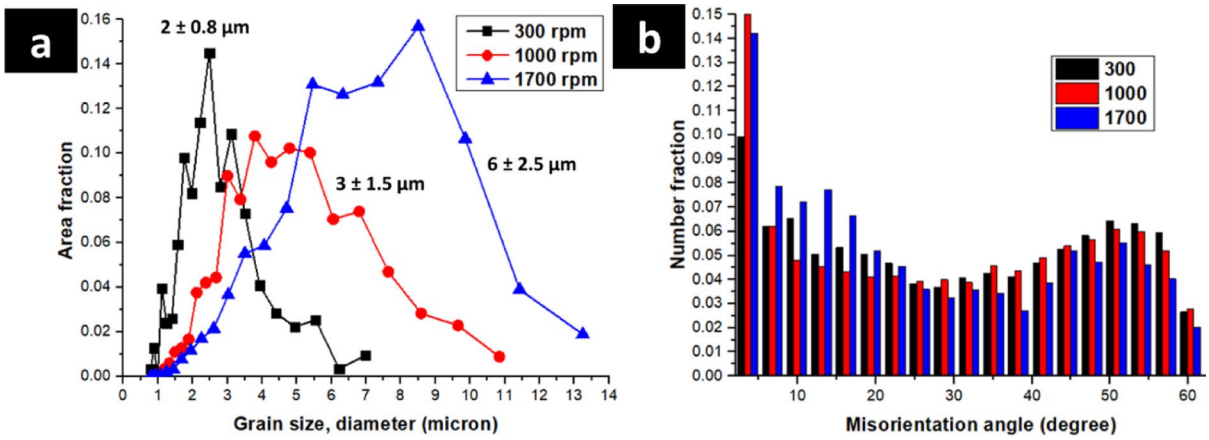

Fig. 12. EBSD-generated graphs from three samples as mentioned in the images showing (**a**) grain size distribution and (**b**) misorientation angle distribution of Al.

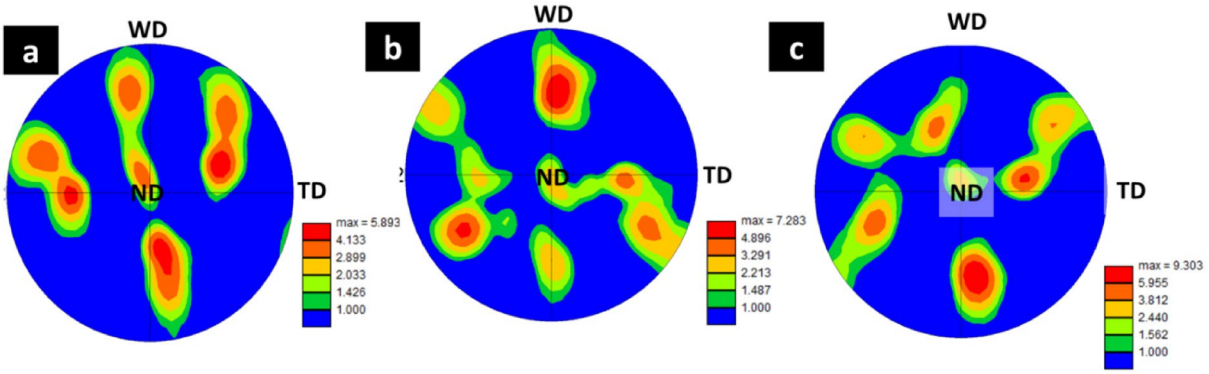

Fig. 13. (111) pole figures representing micro-textures measured from the surface of the weld at different probe rotation speeds of (**a**) 300 rpm, (**b**) 1000 rpm and (**c**) 1700 rpm; WD = welding direction, SPN = shear plane normal, SD = shear direction and ND = normal direction.

component is randomly distributed about this axis[28]. Since FSW is a dynamic deformation process and degree of shear strain/deformation increases with probe rotation speed, recrystallization textures (C-texture) become weaker and shear texture component (A- and B- texture components) become stronger. However, presence of texture components corresponding to ideal shear deformation and non-existence of Cube component of face-centered cubic (FCC) materials confirms the occurrence of CDRX. Prangnell et al.[29]. proposed that the **B** texture component evolved from the **C** texture component with an increase in the induced strain. They further observed that the B texture component dominates the texture at a strain value beyond 25. Montheillet et al.[30] stated that, with an increase in the temperature, the C and $A/\bar{A}$ texture components disappeared progressively and the B texture component became sharper. Therefore, it can be concluded that, at 300 rpm, the temperature of the weld is low and hence both the $A/\bar{A}$ and B texture components are visible in the pole figure (Fig. 11(a)). With an increase in the probe rotation speed, the temperature of the weld increases, resulting in disappearance of the C and $A/\bar{A}$ components and evolution of the B texture component in the weld, as seen in the welds with 1000 rpm (Figure (11(b)) and 1700 rpm (Fig. 11(c)). As the strain in the weld nugget is expected to increase with an increase in the probe rotation speed, the intensity of the dominant texture component increases (as expected). From a comparison of the texture pattern and intensity (Fig. 13), it can be deduced that the strain in the weld nugget material, microstructure evolution mechanism and grain orientation are significantly influenced by the probe rotation speed. Such variation in microstructure is expected to influence the deformation behavior of materials during tensile testing, thereby affecting the mechanical properties of the weld.

Phase evolution

Figure 14 exhibits the X-ray diffraction patterns from the weld at different probe rotation speeds. The joint interface was positioned at the center of the area that was exposed to the XRD beam in order to identify phase evolution at the center of the weld. The patterns indicated the presence of the intermetallic compound $AlFe_3$ in all the welds. The weld corresponding to the 1700 rpm rotation speed exhibited prominent intermetallics peaks. It was found that the intensity of intermetallics (IMC) peaks increases with an increase in the probe rotation

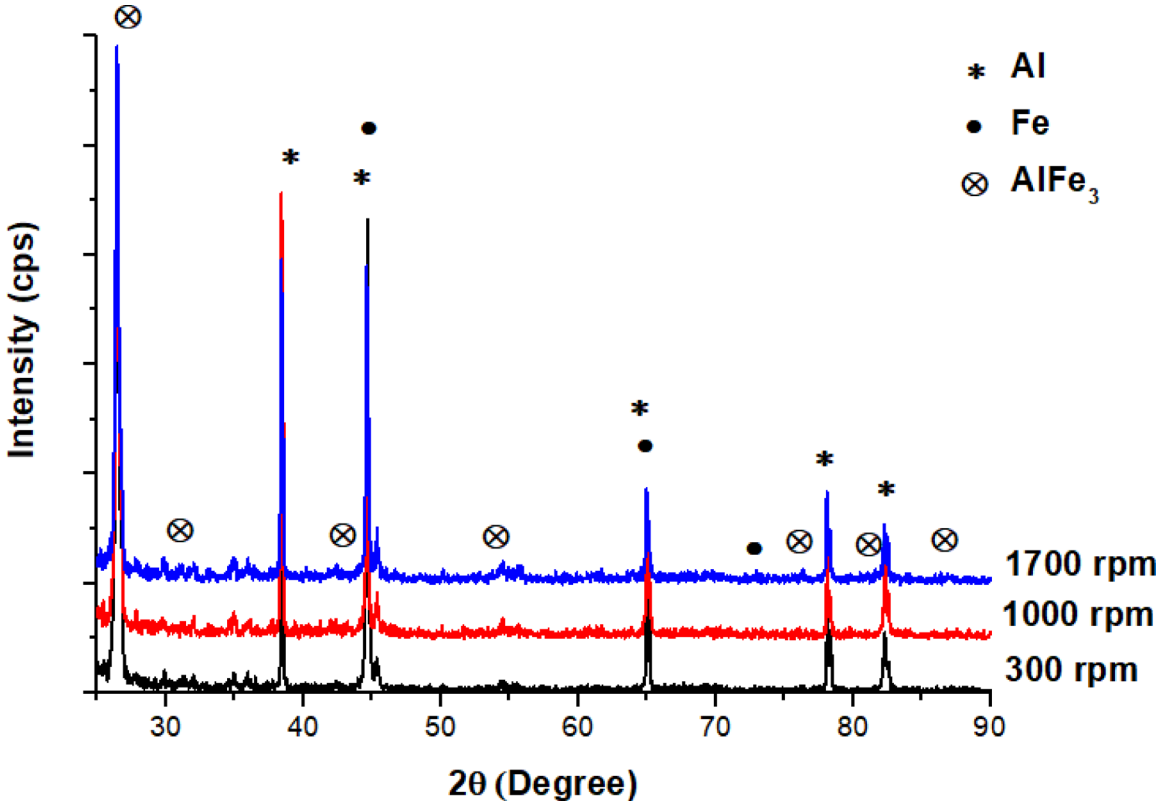

Fig. 14. X-ray diffraction patterns of welds with different probe rotation speeds as mentioned in the figure. Spot size of the incident X-ray is 1 mm in diameter.

speed. It should be noted here that the temperature of the weld interface plays an important role in the quality of joining[31,32]. A higher interface temperature results in wetting of the plasticized Al on a comparatively solid Fe surface; this promotes elemental inter-diffusion and interfacial reaction on the Al side of the weld[33]. This reaction also depends on the local Al: Fe ratio, which varies with the morphology of the interface. For example, the Al: Fe ratio is approximately constant across the interface at 300 rpm while it varies with the location of mechanical mixing in the case of 1700 rpm (Fig. 5 (c)).

The diffusion process is not only activated by thermal deformation but also by strain deformation; severe deformation could influence phase formation in the weld. Li et al.[34] reported that the severe deformation-stimulated (strain induced) diffusion coefficient is about 10^5 higher than that activated by thermal deformation. This is due to the generation of many vacancies during the deformation process. These vacancies could induce significant atomic diffusion during a large deformation process as a consequence of the high thermal and stress coupled effect. For example, enhanced diffusion phenomena have been noticed in mechanical alloying[35], ultrasonic welding[1], friction stir processing[36] and friction stir welding[15]. Therefore, the evolution of intermetallic compounds in the present study is attributed to mechanical mixing, severe deformation at the weld interface and subsequent elemental diffusion at the welding temperature[12].

Mechanical properties

The shear tensile load and elongation of the welds at different probe rotation speeds are presented in Fig. 15(a). It can be seen that the weld corresponding to 1700 rpm exhibits highest shear load. The elongation keeps reducing with an increase in the probe rotation speed. To predict the mode of fracture of the samples, a fractography of the welds with probe rotation speeds of 300 rpm, 1000 rpm and 1700 rpm was done, as shown in Fig. 15(b), 13(c) and 13(d), respectively. The Fig. 15(b) exhibited a brittle mode of fracture (indicated by yellow dotted lines), whereas both ductile (enclosed by circles) and brittle modes of fracture were evident in Fig. 15(c). The results located the fracture at the joint interface and intercalated interface of the welds with 300 rpm and 1000 rpm respectively. Interestingly, a large number of fine dimples (indicated by circles) were noticed in Fig. 15(d), representing fracture in the mechanically mixed zone at a probe rotation speed of 1700 rpm.

It is important to analyze the fracture behavior of a tensile sample and the factors that influence its mechanical properties. The interfacial structure, grain size, and texture are essential parameters that influence the mechanical properties of the weld nugget[37], and understanding the mechanism associated with their variation is crucial for improving the weld quality and reliability[25].

Figure 5 shows interfacial structures at different tool rotational speeds, and three types of interfacial structures are identified, as schematically shown in Fig. 16. The quality and chemical composition of the interface play a significant role in fracture location and tensile properties of the weld, particularly in the case of the weld with

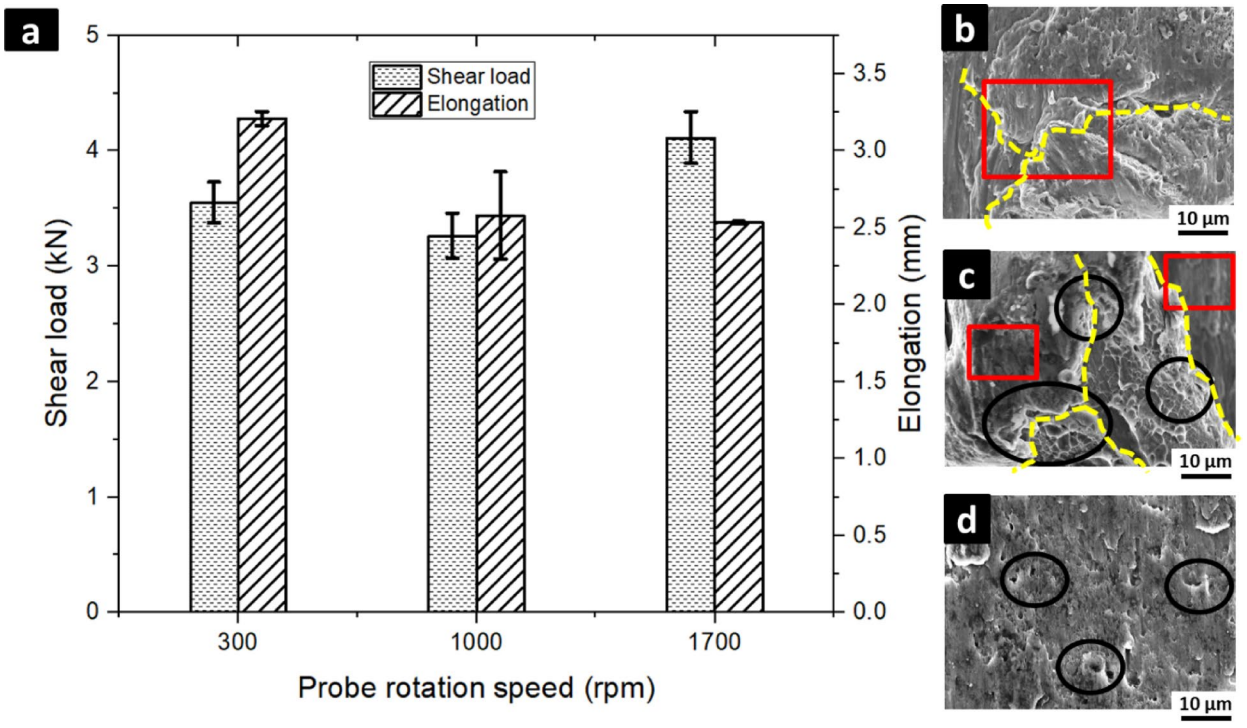

Fig. 15. (**a**) Tensile properties (shear load and elongation) of welds and fractography analysis of welds corresponding to (**b**) 300 rpm, (**c**) 1000 rpm and (**d**) 1700 rpm.

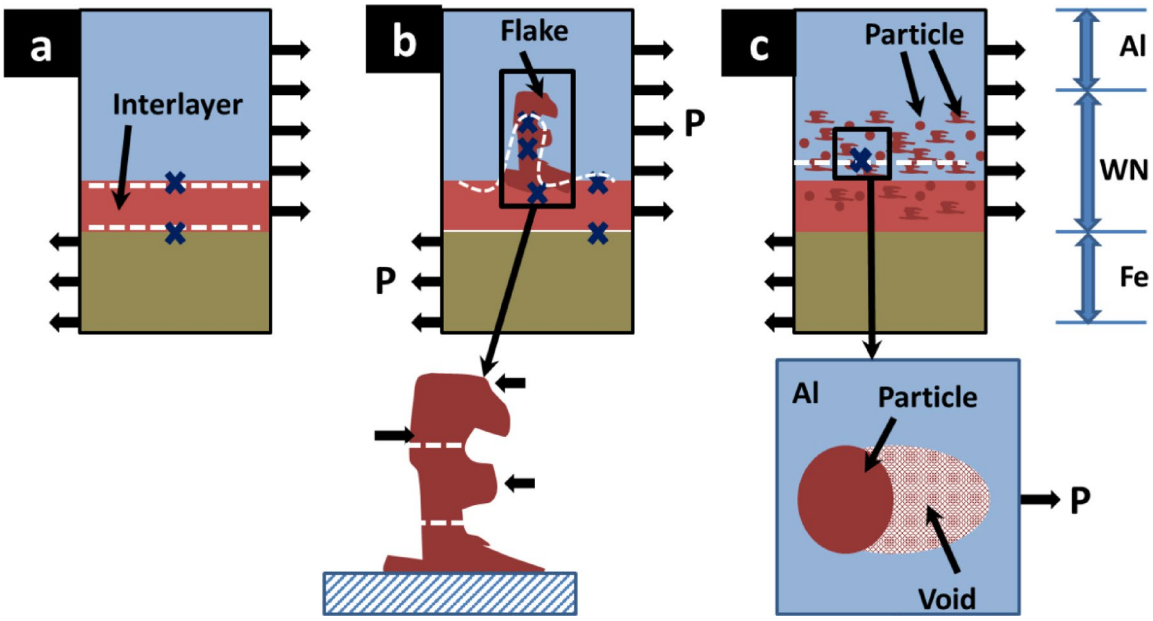

Fig. 16. Schematic representation of three type of weld structure; weld nugget with (**a**) interlayer, (**b**) flakes and (**c**) mechanically mixed zone. Deformation nature of (**d**) flake and (**e**) particle during tensile testing is also represented.

the formation of an interlayer (Fig. 16(a)). Heat input and temperature of the weld influence the thickness of intermetallics in the interlayer (Fig. 14 Figs. 5 and 14), which increases with an increase in heat input that varies with probe rotation speed[38]. The interlayer/Fe and interlayer/Al interfaces are the two critical zones for fracture under the action of the shear tensile test. Since the tensile properties of steel are superior to that of aluminum, aluminum is subjected to more deformation in the weld nugget, and interlayer/Al interface fractures due to incompatibility at the interface due to high differences in deformation.

The morphology and thickness of the interlayer vary along with the interface, and micro-cracks and intercalation are commonly found in the interface[39], which initiates the formation of void and cracks, leading to fracture of the shear tensile sample. Fracture along the interface exhibits brittle type fracture (Fig. 15(b)), and the presence of brittle intermetallic compounds at the location of fracture results in an improvement in tensile strength but a reduction in ductility as per the spring model proposed by Kar et al.[25]. The fraction of intermetallics in the weld nugget corresponding to 300 rpm is very low, and a thin layer of intermetallics is formed. Aluminum is supposed to deform during shear loading, but the Hall–Petch relation predicts that the tensile strength increases as the grain size decreases[40]. Therefore, improved tensile properties at a probe rotation speed of 300 rpm were noticed, as observed in Fig. 13(a).

In the case of a weld with an interlayer and Fe flake, as shown in Fig. 16(b), flake has varying thickness and morphology along its length, and there are several critical locations where it can fracture under the action of shear load due to the uneven morphology of the flakes. The flake behaves as a cantilever beam, with one end fixed to the interlayer adjacent to the Fe side of the weld, and the other end located in the aluminum matrix in the weld nugget. During deformation of aluminum, the shear load is applied to the flake, and the critical locations (thin dimension in flake) are marked with white dotted lines, which are potential locations for crack formation. The critical thickness of the flake causes stress concentration due to higher shear force and bending moment, leading to the premature formation of void and easy crack propagation through the flakes. As a result, the fracture surface looks wavy in morphology (Fig. 15(c)), and premature failure of the testing sample reduces tensile strength. At 1000 rpm, the intermetallics fraction and grain size increase compared to the weld with 300 rpm, which leads to a reduction in shear tensile load, as noticed in Fig. 15(a). This suggests that an increase in intermetallics fraction and grain size reduces the tensile strength of the weld.

In the third case (Fig. 16(c)), the weld nugget composes of fine particles and interlayers. The fine particles are composed of intermetallic compounds that increase the overall fraction of intermetallic compounds (Fig. 14) and enhance the tensile strength and brittleness of particles. However, these particles are distributed in the aluminum matrix and hence, the weld nugget resembles a dispersion induced composite (Fig. 5). During shear deformation, particles in the weld nugget restrict the dislocation glide and easy deformation of aluminum. At the critical load, strain mismatch between aluminum matrix and particle results in the formation of a void. Propagation[41] and coalescence of these voids along the line of maximum stress leads to failure of the testing sample. Each void in aluminum matrix develops a dimple in the fracture sample, as shown in Fig. 15(d). Higher mechanical properties of the weld nugget at 1700 rpm (Fig. 15(a)) is attributed to the structural superiority and formation of the mechanically mixed zone, as schematically shown in Fig. 16(c).

Although the weld corresponding to 1700 rpm (limitation of current welding system) exhibited the highest shear strength, further increases in probe rotation speed may lead to a negative impact on mechanical properties. Excessive probe rotational speed can induce severe plastic deformation and interface fragmentation from the Fe interface, which could increase the likelihood of tool wear or breakage of the probe due to high hardness and strength of steel. Additionally, localized temperature rise at the interface may cause incipient melting of Al, which is expected to enhance interfacial diffusion and potentially result in the formation of a higher fraction of IMCs through partial melting. These undesirable effects may compromise joint ductility and toughness. A quantitative assessment of the individual roles of fractured Fe particles and intermetallic compounds in contributing to joint performance will be the subject of a future study.

Conclusions

In the present investigation, a friction stir lap welding of Al 6061-T6 alloy and mild steel was carried out at three different probe rotation speeds keeping shoulder rotation speed fixed to maintain constant heat input and increase deformation adjacent to weld interface using adjustable tool. The effect of probe rotation speed on the microstructure and elemental mixing at the Al/Fe interface during friction stir welding has been investigated. Based on detailed investigations, the following conclusions were drawn:

1. Probe rotation speed has a significant effect on the deformation, fragmentation, and elemental mixing at the interface. Higher probe rotation speeds lead to more severe deformation and fragmentation of the Fe interface, as well as the formation of zones of elemental mixing. Three different types of weld interfaces were identified due to the change in probe rotation speed. The lower amount of deformation at a low probe rotation speed leads to the formation of an interface without an extended interlayer, whereas a higher probe rotation speed develops an intercalated interface and results in substantial mechanical mixing at the interface. Such mechanical mixing was absent in the weld with lower probe rotation speed.
2. The microstructural evolution at the weld interface is influenced by several micro-mechanisms. Continuous dynamic recrystallization is the likely mechanism of microstructural evolution in aluminum, whereas the deformation of steel (Fe side of the interface) takes place by the conventional shear mode. The probe rotation speed strongly influences on the deformation of Fe at the interface, resulting in the formation of different types of interface structures.
3. The dissimilar weld with 1700 rpm exhibited the highest shear load. The elongation of the welds decreased progressively with an increase in the probe rotation speed. Such a variation in weld quality is attributed to the transition in interfacial structure and morphology.
4. The fractography analysis pointed out both ductile and brittle modes of fracture in all the welds. However, their relative fraction and spatial distribution varied with the probe rotation speed. A transition in the mechanism of tensile fracture of the weld from brittle to the ductile mode of fracture with an increase in probe rotation speed was noticed. Such transition was attributed to the variation in the interfacial structure of the dissimilar weld. The formation of a mechanically mixed zone was responsible for the higher shear tensile property of the weld with higher probe rotation speed.

5. The intermetallic compounds present in the weld nugget significantly affect the mechanical properties of the weld. The weld with fine particles and interlayers exhibited higher mechanical properties than the welds without an extended interlayer or with uneven distribution of particles.
6. The study provides insights into the role of probe rotation speed in controlling interface morphology, mechanical mixing, and joint performance using an adjustable tool. The findings of this study can be used to improve processing strategies for structurally reliable Al/Fe joints in various industrial applications.

Data availability

The datasets generated during and/or analysed during the current study are not publicly available due to ongoing research but are available from the corresponding author on reasonable request.

Received: 17 March 2025; Accepted: 18 July 2025
Published online: 27 July 2025

References

1. Li, H. et al. Interfacial reactions and joint performances of high-power ultrasonic welding of aluminum to steel. *J. Mater. Res. Technol.* **26**, 328–343. https://doi.org/10.1016/j.jmrt.2023.07.188 (2023).
2. Chu, Q. et al. Interfacial investigation of explosion-welded al/steel plate: the microstructure, mechanical properties and residual stresses. *Mater. Sci. Engineering: A*. **833**, 142525. https://doi.org/10.1016/j.msea.2021.142525 (2022).
3. Khan, F., Miura, T., Morisada, Y., Ushioda, K. & Fujii, H. Dissimilar joining of A7075 aluminum and SS400 steel utilizing center-driven double-sided linear friction welding using mild steel as a center material: processing, mechanical and microstructure characterization. *J. Manuf. Process.* **139**, 67–80. https://doi.org/10.1016/j.jmapro.2025.02.017 (2025).
4. Khan, F. et al. Sound dissimilar linear friction welding of A7075-T6 al and mild steel by simultaneous interfacial deformation using higher forging speed. *J. Manuf. Process.* **109**, 512–523. https://doi.org/10.1016/j.jmapro.2023.12.023 (2024).
5. Kar, A. et al. Mechanism of joint formation in dissimilar friction stir welding of aluminum to steel, in: : pp. 237–245. (2023). https://doi.org/10.1007/978-3-031-22661-8_22
6. Sharma, A., Morisada, Y. & Fujii, H. Investigation of through-thickness microstructural evolution and mechanical properties variation in friction stir alloyed Al-Fe alloy system. *J. Alloys Compd.* **921**, 166154. https://doi.org/10.1016/j.jallcom.2022.166154 (2022).
7. Wang, X., Morisada, Y. & Fujii, H. High-strength fe/al dissimilar joint with uniform nanometer-sized intermetallic compound layer and mechanical interlock formed by adjustable probes during double-sided friction stir spot welding. *Mater. Sci. Engineering: A*. **809**, 141005. https://doi.org/10.1016/j.msea.2021.141005 (2021).
8. Liu, H., Morisada, Y. & Fujii, H. Friction stir welding: process, temperature, microstructure and properties. *Sci. Technol. Weld. Joining*. **28**, 619–632. https://doi.org/10.1080/13621718.2023.2229025 (2023).
9. Jabraeili, R. et al. Effect of FSW process parameters on microstructure and mechanical properties of the dissimilar AA2024 al alloy and 304 stainless steel joints. *Mater. Sci. Engineering: A*. **814**, 140981. https://doi.org/10.1016/j.msea.2021.140981 (2021).
10. Wang, X. & Lados, D. A. Optimization of aluminum-to-steel friction stir lap welding for the fabrication of high-integrity structural components. *J. Adv. Join. Processes*. **5**, 100114. https://doi.org/10.1016/j.jajp.2022.100114 (2022).
11. Zhang, W., Liu, H., Ding, H. & Fujii, H. Grain refinement and superplastic flow in friction stir processed Ti–15V–3Cr–3Sn–3Al alloy. *J. Alloys Compd.* **803**, 901–911. https://doi.org/10.1016/j.jallcom.2019.06.323 (2019).
12. Kar, A., Kailas, S. V. & Suwas, S. Effect of mechanical mixing in dissimilar friction stir welding of aluminum to titanium with zinc interlayer. *Trans. Indian Inst. Met.* **72**, 1533–1536. https://doi.org/10.1007/s12666-019-01643-x (2019).
13. Sharma, A., Morisada, Y., Nagaoka, T. & Fujii, H. Influence of the number of FSP passes on the strength-ductility synergy of cold-rolled spark plasma sintered pure aluminum. *J. Manuf. Process.* **79**, 296–304. https://doi.org/10.1016/j.jmapro.2022.04.061 (2022).
14. Wang, T. et al. Effect of Hook characteristics on the fracture behaviour of dissimilar friction stir welded aluminium alloy and mild steel sheets. *Sci. Technol. Weld. Joining*. **24**, 178–184. https://doi.org/10.1080/13621718.2018.1503801 (2019).
15. Kar, A., Kailas, S. V. & Suwas, S. Effect of zinc interlayer in microstructure evolution and mechanical properties in dissimilar friction stir welding of aluminum to titanium. *J. Mater. Eng. Perform.* **27**, 6016–6026. https://doi.org/10.1007/s11665-018-3697-8 (2018).
16. Zhang, M. et al. High-quality dissimilar friction stir welding of al to steel with no contacting between tool and steel plate. *Mater. Charact.* **191**, 112128. https://doi.org/10.1016/j.matchar.2022.112128 (2022).
17. Sharma, A., Morisada, Y. & Fujii, H. Interfacial microstructure and strengthening mechanisms of spsed al/gnp nanocomposite subjected to multi-pass friction stir processing. *Mater. Charact.* **197**, 112652. https://doi.org/10.1016/j.matchar.2023.112652 (2023).
18. Wang, X. et al. Interface structure and mechanical properties of fe/al dissimilar lap joints formed by friction stir welding using an adjustable tool. *Sci. Technol. Weld. Joining*. **28**, 701–709. https://doi.org/10.1080/13621718.2023.2210980 (2023).
19. Kar, A., Vicharapu, B., Morisada, Y. & Fujii, H. Elucidation of interfacial microstructure and properties in friction stir lap welding of aluminium alloy and mild steel. *Mater. Charact.* **168**, 110572. https://doi.org/10.1016/j.matchar.2020.110572 (2020).
20. Liu, Z., Ji, S. & Meng, X. Improving joint formation and tensile properties of dissimilar friction stir welding of aluminum and magnesium alloys by solving the pin adhesion problem. *J. Mater. Eng. Perform.* **27**, 1404–1413. https://doi.org/10.1007/s11665-018-3216-y (2018).
21. Soni, P. R. *Mechanical Alloying: Fundamentals and Applications* (Cambridge International Science Publishing, 2000).
22. Kar, A. et al. A new method to elucidate fracture mechanism and microstructure evolution in titanium during dissimilar friction stir welding of aluminum and titanium. *Mater. Charact.* **171**, 110791. https://doi.org/10.1016/j.matchar.2020.110791 (2021).
23. Kesharwani, R., Imam, M. & Sarkar, C. Clarification on the choice of sheet positioning in friction stir welding of dissimilar materials. *Manuf. Lett.* **24**, 100–104. https://doi.org/10.1016/j.mfglet.2020.04.008 (2020).
24. Khodabakhshi, F. & Gerlich, A. P. Potentials and strategies of solid-state additive friction-stir manufacturing technology: A critical review. *J. Manuf. Process.* **36**, 77–92. https://doi.org/10.1016/j.jmapro.2018.09.030 (2018).
25. Kar, A., Suwas, S. & Kailas, S. V. Two-pass friction stir welding of aluminum alloy to titanium alloy: A simultaneous improvement in mechanical properties. *Mater. Sci. Engineering: A*. **733**, 199–210. https://doi.org/10.1016/j.msea.2018.07.057 (2018).
26. Salih, O. S., Ou, H. & Sun, W. Heat generation, plastic deformation and residual stresses in friction stir welding of aluminium alloy. *Int. J. Mech. Sci.* **238**, 107827. https://doi.org/10.1016/j.ijmecsci.2022.107827 (2023).
27. Klepaczko, J. R. & Rezaig, B. A numerical study of adiabatic shear banding in mild steel by dislocation mechanics based constitutive relations. *Mech. Mater.* **24**, 125–139. https://doi.org/10.1016/S0167-6636(96)00039-7 (1996).
28. Hu, Y., Liu, H. & Fujii, H. Improving the mechanical properties of 2219-T6 aluminum alloy joints by ultrasonic vibrations during friction stir welding. *J. Mater. Process. Technol.* **271**, 75–84. https://doi.org/10.1016/j.jmatprotec.2019.03.013 (2019).
29. Prangnell, P. B. & Heason, C. P. Grain structure formation during friction stir welding observed by the 'stop action technique'. *Acta Mater.* **53**, 3179–3192. https://doi.org/10.1016/j.actamat.2005.03.044 (2005).

30. Montheillet, F., Cohen, M. & Jonas, J. J. Axial stresses and texture development during the torsion testing of al, Cu and α-Fe. *Acta Metall.* **32**, 2077–2089. https://doi.org/10.1016/0001-6160(84)90187-1 (1984).
31. Geng, P. et al. Prediction of residual stresses within dissimilar al/steel friction stir lap welds using an Eulerian-based modeling approach. *J. Manuf. Process.* **79**, 340–355. https://doi.org/10.1016/j.jmapro.2022.05.001 (2022).
32. Geng, P. et al. Effects of rotation tool-induced heat and material flow behaviour on friction stir lapped al/steel joint formation and resultant microstructure. *Int. J. Mach. Tools Manuf.* **174**, 103858. https://doi.org/10.1016/j.ijmachtools.2022.103858 (2022).
33. Sun, Y. F., Fujii, H., Takaki, N. & Okitsu, Y. Microstructure and mechanical properties of dissimilar al alloy/steel joints prepared by a flat spot friction stir welding technique. *Mater. Des.* **47**, 350–357. https://doi.org/10.1016/j.matdes.2012.12.007 (2013).
34. LI, R. et al. Friction heat production and atom diffusion behaviors during Mg-Ti rotating friction welding process. *Trans. Nonferrous Met. Soc. China*. **22**, 2665–2671. https://doi.org/10.1016/S1003-6326(11)61515-X (2012).
35. Sharma, A. et al. Investigating the diffusion behavior in the Ti-Fe, Ni-Ti, Ti-Al, and Ni-Al binary systems during solid-state synthesis of intermetallic compounds via mechanical alloying. *J. Alloys Compd.* **1022**, 179964. https://doi.org/10.1016/j.jallcom.2025.179964 (2025).
36. Qian, J., Li, J., Xiong, J., Zhang, F. & Lin, X. Situ synthesizing Al3Ni for fabrication of intermetallic-reinforced aluminum alloy composites by friction stir processing. *Mater. Sci. Engineering: A*. **550**, 279–285. https://doi.org/10.1016/j.msea.2012.04.070 (2012).
37. Zhang, C., Huang, G. & Liu, Q. Quantitative analysis of grain structure and texture evolution of dissimilar AA2024/7075 joints manufactured by friction stir welding. *Mater. Today Commun.* **26**, 101920. https://doi.org/10.1016/j.mtcomm.2020.101920 (2021).
38. Sharma, A., Morisada, Y., Ushioda, K. & Fujii, H. Elucidation on the correlation between thermal stability of Al13Fe4 intermetallic phase and mechanical properties of the Al-Fe alloy fabricated via friction stir alloying. *J. Alloys Compd.* **967**, 171732. https://doi.org/10.1016/j.jallcom.2023.171732 (2023).
39. Choi, J. W., Liu, H. & Fujii, H. Dissimilar friction stir welding of pure Ti and pure al. *Mater. Sci. Engineering: A*. **730**, 168–176. https://doi.org/10.1016/j.msea.2018.05.117 (2018).
40. Hansen, N. Hall–Petch relation and boundary strengthening. *Scr. Mater.* **51**, 801–806. https://doi.org/10.1016/j.scriptamat.2004.06.002 (2004).
41. Wang, L. et al. Sandwich-Like cu/al/cu composites fabricated by Cryorolling. *Adv. Eng. Mater.* **22** https://doi.org/10.1002/adem.202000122 (2020).

Acknowledgements

This work is supported by a Grant-in-Aid for Scientific Research (Kakenhi) from the Japan Society for Promotion of Science (Grant Number 24K17532) and JST-Mirai Program (Grant Number JPMJMI19E5), Japan.

Author contributions

AK- Investigation, Formal analysis, writing-original draftYM- Supervision, Validation, ReviewAS- Validation, Funding acquisition, EditingHF- Project management, Funding acquisition, Editing.

Declarations

Competing interests

AS - The corresponding author (AS) is an Editorial Board Member for this journal and was not involved in the editorial review or the decision to publish this article.AK - The author declare that they have no known competing financial interests or personal relationships that could have appeared to influence the work reported in this paperYM - The author declare that they have no known competing financial interests or personal relationships that could have appeared to influence the work reported in this paperHF - The author declare that they have no known competing financial interests or personal relationships that could have appeared to influence the work reported in this paper.

Additional information

Correspondence and requests for materials should be addressed to A.S. or H.F.

Reprints and permissions information is available at www.nature.com/reprints.

Publisher's note Springer Nature remains neutral with regard to jurisdictional claims in published maps and institutional affiliations.